Fluid Dynamics in the HeartMate 3: Influence of the Artificial Pulse Feature and Residual Cardiac Pulsation

Wiegmann, Lena ; Thamsen, Bente ; de Zélicourt, Diane ; Granegger, Marcus ; Boës, Stefan ; Schmid Daners, Marianne ; Meboldt, Mirko ; Kurtcuoglu, Vartan

Abstract: Ventricular assist devices (VADs), among which the HeartMate 3 (HM3) is the latest clinically approved representative, are often the therapy of choice for patients with end-stage heart failure. Despite advances in the prevention of pump thrombosis, rates of stroke and bleeding remain high. These complications are attributed to the flow field within the VAD, among other factors. One of the HM3's characteristic features is an artificial pulse that changes the rotor speed periodically by 4000 rpm, which is meant to reduce zones of recirculation and stasis. In this study, we investigated the effect of this speed modulation on the flow fields and stresses using high-resolution computational fluid dynamics. To this end, we compared Eulerian and Lagrangian features of the flow fields during constant pump operation, during operation with the artificial pulse feature, and with the effect of the residual native cardiac cycle. We observed good washout in all investigated situations, which may explain the low incidence rates of pump thrombosis. The artificial pulse had no additional benefit on scalar washout performance, but it induced rapid variations in the flow velocity and its gradients. This may be relevant for the removal of deposits in the pump. Overall, we found that viscous stresses in the HM3 were lower than in other current VADs. However, the artificial pulse substantially increased turbulence, and thereby also total stresses, which may contribute to clinically observed issues related to hemocompatibility.

DOI: https://doi.org/10.1111/aor.13346

Fluid dynamics in the HeartMate 3: Influence of the artificial pulse feature and residual cardiac pulsation

Lena Wiegmann[1], Bente Thamsen[2,4], Diane de Zélicourt[1,3], Marcus Granegger[2], Stefan Boës[4], Marianne Schmid Daners[4], Mirko Meboldt[4], Vartan Kurtcuoglu[1,3,5]

Affiliations:

[1] The Interface Group, Institute of Physiology, University of Zurich, Zurich, Switzerland
[2] Pediatric Heart Centre, University Children's Hospital Zurich, Zurich, Switzerland
[3] National Center of Competence in Research, Kidney.CH, Zurich, Switzerland
[4] Product Development Group Zurich, Department of Mechanical and Process Engineering, ETH Zurich, Zurich, Switzerland
[5] Zurich Center for Integrative Human Physiology, University of Zurich, Zurich, Switzerland

Corresponding Author:

Prof. Dr. Vartan Kurtcuoglu
The Interface Group
Institute of Physiology
University of Zurich
Winterthurerstrasse 190
CH-8057 Zürich
Switzerland
Tel: +41 44 635 50 55
Fax: +41 44 635 68 14
vartan.kurtcuoglu@uzh.ch

Abstract

Ventricular assist devices (VADs), among which the HeartMate 3 (HM3) is the latest clinically approved representative, are often the therapy of choice for patients with end-stage heart failure. Despite advances in the prevention of pump thrombi, rates of stroke and bleeding remain high. These complications are attributed to the flow field within the VAD, among other factors. One of the HM3's characteristic features is an artificial pulse that changes the rotor speed periodically by 4000 rpm, which is meant to reduce zones of recirculation and stasis. In this study, we investigated the effect of this speed modulation on the flow fields and stresses using high-resolution computational fluid dynamics. To this end, we compared Eulerian and Lagrangian features of the flow fields during constant pump operation, during operation with the artificial pulse feature and with the effect of the residual native cardiac cycle. We observed good washout in all investigated situations, which may explain the low incidence rates of pump thrombosis. The artificial pulse had no additional benefit on scalar washout performance, but it induced rapid variations in the flow velocity and its gradients. This may be relevant for the removal of deposits in the pump. Overall, we found that viscous stresses in the HM3 were lower than in other current VADs. However, the artificial pulse substantially increased turbulence, and thereby also total stresses, which may contribute to clinically observed issues related to hemocompatibility.

Keywords: ventricular assist devices, HeartMate 3, computational fluid dynamics, artificial pulse, cardiac cycle, hemocompatibility

Introduction

The HeartMate 3 (HM3, Abbott, St. Paul, MN, USA) is the latest clinical ventricular assist device (VAD) designed for long-term support of patients with advanced heart failure. It is characterized by a magnetic levitation system, textured blood-contacting surfaces, wide flow gaps and an artificial pulse [1]. Together, these features shall enhance the hemocompatibility of the pump and reduce thrombotic and hemorrhagic adverse events. Clinical results so far suggest that the HM3 decreases incidence rates of pump thrombosis and stroke compared to the HeartMate 2 (Abbott), while the rates of disabling stroke are similar [2]. Bleeding rates are comparable to other VADs [2,3], even though the HM3 appears to preserve high molecular weight von Willebrand factor (VWF) multimers better than other clinically used VADs [4].

Hemocompatibility is linked to the blood flow within the VAD. This includes regions of stagnation and recirculation that may promote thrombus formation [5], as well as high shear areas that may activate platelets [6] and reduce VWF functionality [7]. It has been hypothesized that the HM3's artificial pulse improves pump washout [1] and thereby inhibits pump thrombus formation. However, this hypothesis has not been tested so far. Further, while rotary blood pumps typically operate at a constant speed, maintaining some pulsatility has been hypothesized to have positive effects on the vasculature [8]. Evidence on the beneficial effect of periodic speed changes has been provided by comparative studies in patients with an HVAD (Medtronic, Minneapolis, MN, USA), which features an optional periodic speed modulation. Patients with the modulation enabled had significantly fewer rates of stroke, sepsis and right heart failure than those without, while overall survival and gastrointestinal bleeding rates were not affected [9].

The HM3's artificial pulse comprises a decrease of the pump speed by 2000 rpm, followed by an increase by 4000 rpm, before operation at nominal speed is resumed. This pulse lasts 350 ms and is repeated every 2 seconds. While the flow inside the HM3 has been investigated under steady conditions [1], the effects of the rapid change in rotor speed on the flow and corresponding stress fields have not. Given the severity of the modulation of pump operation, we view it as imperative to understand its influence on blood flow and to consider effects on blood components along with potential downstream consequences.

To contribute to this understanding, we utilized computational fluid dynamics (CFD) and investigated the haemodynamic characteristics of the artificial pulse in absence of any remaining cardiac function, and of cardiac pulsatility without artificial pulse, comparing both to a baseline with neither native nor artificial pulsatility. Our CFD framework includes high-resolution dynamic flow simulations in the VAD and a lumped parameter representation of the cardiovascular system including the pump. We have analyzed the computed data with respect to Eulerian and Lagrangian characteristics linked to blood damage and thrombosis potential, and juxtaposed the results to clinical findings.

Methods

We simulated three different scenarios: The first one considers a remaining cardiac function and a HM3 operating without the artificial pulse feature with constant speed for a full cardiac cycle (hereinafter referred to as "cardiac cycle"). The second one considers no native heart function, but includes the HM3 artificial pulse ("artificial pulse"). The final one represents the baseline case with constant HM3 speed and no native heart function ("baseline"). We set pump speeds to maintain a mean cardiac output of 5 L/min [10] in all three scenarios. Boundary conditions (BCs) for the flow

computations in the VAD were obtained from a lumped parameter representation of the entire cardiovascular system, including the pump.

Geometry

An explanted HM3 pump was scanned using an X-ray micro computed tomography system (MicroDETECT, Empa, Zurich, Switzerland) as in [11]. The resulting pixel size was 30 µm. The obtained images were segmented using Mimics (Materialise, Leuven, Belgium) and reconstructed in Solidworks (Dassault Systèmes, Waltham MA, USA). The identified top and bottom gaps between rotor and housing are 1mm and 1.75mm, respectively.

Computational fluid dynamic simulations

CFD simulations were carried out using StarCCM+ (Siemens, Munich, Germany). Polyhedral grids were generated for all parts of the domain except inlet and outlet cannulas, including an eight-element boundary layer along the walls in the rotating part and a ten-element boundary layer in the volute. Local mesh refinement was performed where needed. A 7cm extension was added to the outlet cannula to avoid spurious influence of the boundary conditions on the domain of interest. Inlet cannula and outlet cannula plus graft extension were discretized using a directed mesh. The final grid contained 9.95 million cells.

The three-dimensional unsteady Reynolds-averaged Navier-Stokes equations were solved using implicit second order temporal and spatial discretization, a segregated flow approach and k-ω-SST turbulence modeling. Inlet turbulent boundary conditions were prescribed based on relationships for fully developed turbulent pipe flow, namely turbulent intensity = $0.16 \cdot Re^{1/8} = 0.06$ and turbulent length scale = $0.07 \cdot D = 1.33$ mm, with D being the diameter of the inlet cannula. Blood was modelled as a Newtonian fluid with a viscosity of 3.5 mPa·s and a density of 1050 kg/m^3. This simplification was considered acceptable, as the non-Newtonian properties of blood, such as shear-thinning, become negligible at high shear rates (> 100 s^{-1}) [12] such as those typically found in VADs. The rotation of the impeller was implemented as a rigid body motion. Pressure boundary conditions were prescribed at the inlet and outlet. For the cardiac cycle and artificial pulse simulations, the time-dependent pressure BCs were obtained from the corresponding lumped-parameter simulations.

All simulations were carried out with a convergence criterion of 10^{-5} for the residual errors and a time step corresponding to 2° of rotation. For the artificial pulse, the time step was kept constant at the smaller value during the ramping time, corresponding to 2° at the higher speed. Grid and time step independence were confirmed for pressure, velocity, and shear stresses as reported in the supporting information.

Lumped parameter model

Pressure BCs were obtained from a lumped parameter model of the entire circulation, including a mathematical representation of the dynamic response of the HM3. A numerical model similar to previously reported ones [13–16] was employed to simulate the cardiovascular system. Arterial and venous vasculatures were modeled as 3- and 2-element Windkessel models [17], respectively. The heart was modeled as having a time-varying elastance with nonlinear end-diastolic/end-systolic pressure-volume relationships and unidirectional valves as suggested in Colacino et al. [13]. End-diastolic pressure-volume relationship and elastance were adapted based on [10] and [18] to mimic the cardiac function of a typical LVAD patient. Cardiovascular parameters were adapted to mimic the ones of an average LVAD patient [10] resulting in an end-diastolic left ventricular volume of 345 mL and an ejection fraction of 10.3 % pre-implantation. The mathematical representation of the HM3 was derived from in vitro experiments similar to [19,20]. The in vitro experiments were conducted on the

mock loop setup described in [21] using a glycerol-water mixture with a viscosity of 3.0 ± 0.1 mPa·s, corresponding to a hematocrit of 31 %. A 15 cm long outlet graft, which is within the range of graft lengths found in patients [22], was included as hydraulic resistance and inertance between the pump outlet and aorta. That graft was subdivided into two compartments, respectively accounting for the first 7 cm and subsequent 8 cm of the graft, allowing for the extraction of the pressure boundary conditions 7 cm away from the pump corresponding to the outlet extension included in the CFD simulations.

Simulation "baseline"

In the baseline case, we investigated the flow in the HM3 at a constant speed and no influence of the native circulation. The pump was operated at 5650 rpm and 80 mmHg. For assessment of the washout performance, CFD calculations were carried out for 40 full rotations.

Simulation "cardiac cycle"

In the cardiac cycle simulation, the HM3 was run at a constant speed of 5250 rpm and the effect of physiologic pressure pulsations induced by native heart function on the flow field within the VAD were investigated. Appropriate dynamic behavior was ensured by initialization over two full cardiac cycles, run with a time step of 4° to reduce computational effort. After initialization, one full cardiac cycle (0.658 s at 91.2 bpm [10] , corresponding to approximately 58 full rotations) was calculated with a time step size corresponding to 2°.

Simulation "artificial pulse"

In the artificial pulse simulation, the effect of the HM3 speed modulation on the flow field within the VAD was investigated. The system was initialized at 5650 rpm and a flow of 5 L/min, before the speed and pressure BCs including the speed change were prescribed for a total duration of 670 ms, corresponding to approximately 59 full rotations.

Analyses

We analyzed various Eulerian and Lagrangian features of the flow field both qualitatively and quantitatively. We calculated the scalar viscous shear stress, τ_{visc}, from the viscous shear stress components, σ_{ij}, according to [23,24]:

$$\tau_{visc} = \left[\frac{1}{12}\sum\left(\sigma_{ii} - \sigma_{jj}\right)^2 + \frac{1}{2}\sum \sigma_{ij}^2\right]^{1/2} \quad (1)$$

Similarly, we calculated a scalar total shear stress, τ_{tot}, including turbulent stresses as

$$\tau_{tot} = \left[\frac{1}{12}\sum\left((\sigma_{ii} + s_{ii}) - (\sigma_{jj} + s_{jj})\right)^2 + \frac{1}{2}\sum\left(\sigma_{ij} + s_{ij}\right)^2\right]^{1/2}, \quad (2)$$

with the components of the Reynolds stress tensor s_{ij} given by

$$s_{ij} = -\rho \cdot \overline{u_i' u_j'} = -\frac{2}{3}\rho k \delta_{ij} + \mu_t \left(\frac{\partial u_i}{\partial x_j} + \frac{\partial u_j}{\partial x_i}\right), \quad (3)$$

where ρ is density, $u'$is the fluctuating component of the mean fluid velocity, k is turbulent kinetic energy, δ_{ij} is the Kronecker delta, μ_t is turbulent viscosity and u is mean fluid velocity.

To probe blood cell paths through the pump, we implemented Lagrangian particle tracking with passive advection. The tracked particles had a diameter of 5 µm and a density of 1125 kg/m^3, which are

representative of, respectively, the dimension and density of red blood cells. At least 798 particles were seeded 44 mm downstream of the inlet with uniform spatial distribution at multiple instances in time. We confirmed that the derived metric (exposure time to stress above a specific threshold) did not depend on the number of tracked particles (supporting information).

To investigate washout, we quantified advection of a passive scalar Φ:

$$\rho\frac{\partial\phi}{\partial t} + \rho\nabla\cdot(u\phi) = S_\phi(t)$$
$$S_\phi(t) = \begin{cases} 100\,, t = t_0 \\ 0, t \neq t_0 \end{cases} \quad (4)$$

where t is time, S_Φ is a source term and t_0 is the scalar initialization time.

Results

Hydraulic data

To confirm that the imposed BCs result in the desired fluid dynamic behavior, we compared the flow curves obtained with CFD to corresponding data obtained using the lumped parameter model (Figure 1). Overall, the CFD and LP model data agree well (root mean square error of 6% and 10% for the cardiac cycle and artificial pulse, respectively). The arterial pulse pressures in the cardiac cycle and artificial pulse simulations are 5 mmHg and 11 mmHg, respectively.

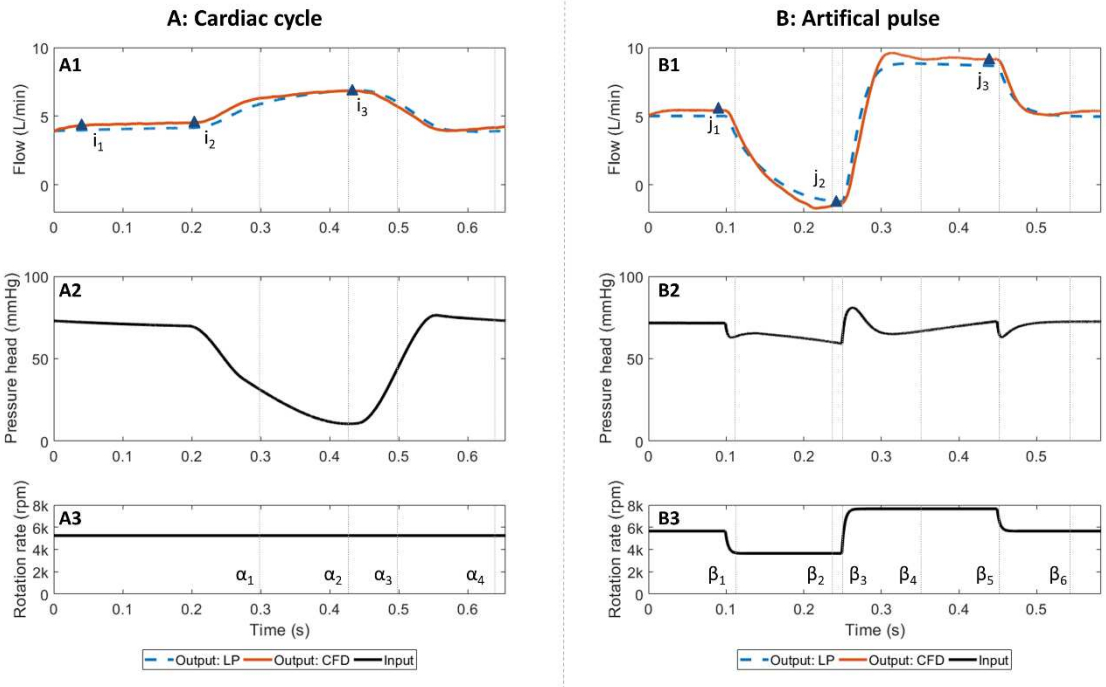

Figure 1: Calculated flow rates and corresponding model input in the 'cardiac cycle' (Panels A) and 'artificial pulse' scenarios (Panels B). Flow rates calculated using the lumped parameter (LP) and CFD models are shown in Panels 1 (dashed and solid lines, respectively). Pressure head and rotation rate were prescribed as model input (Panels 2 and 3). α_1- α_4 and β_1- β_6 indicate time points selected to visualize the flow structures in subsequent figures. i_1-i_3 and j_1-j_3 indicate injection time points for Lagrangian particles highlighted in Figure 5.

Flow field (velocity & vorticity)

To understand flow features inside the pump, we started by investigating the 'baseline' scenario (constant speed and constant BCs). Here, areas of flow detachment are observed at the pressure side and the trailing edges of the blades (Figure 2B, markers I & II). An area of stagnation forms centrally under the rotor (III). Vorticity is increased in regions of recirculation or flow detachment at the pressure side and trailing edges of the blade, in the gaps (IV), as well as at the tongue (V), depending on blade position (Figure 2D). In addition, we observe flow features similar to a wavy vortex flow in the side gap between rotor and housing (Figure 2C). The regions of flow detachment and wavy vortex pattern remain present during the entire rotation and occur at all tested quasi-steady flow situations (incl. the high flow/high speed plateau in the 'artificial pulse' scenario).

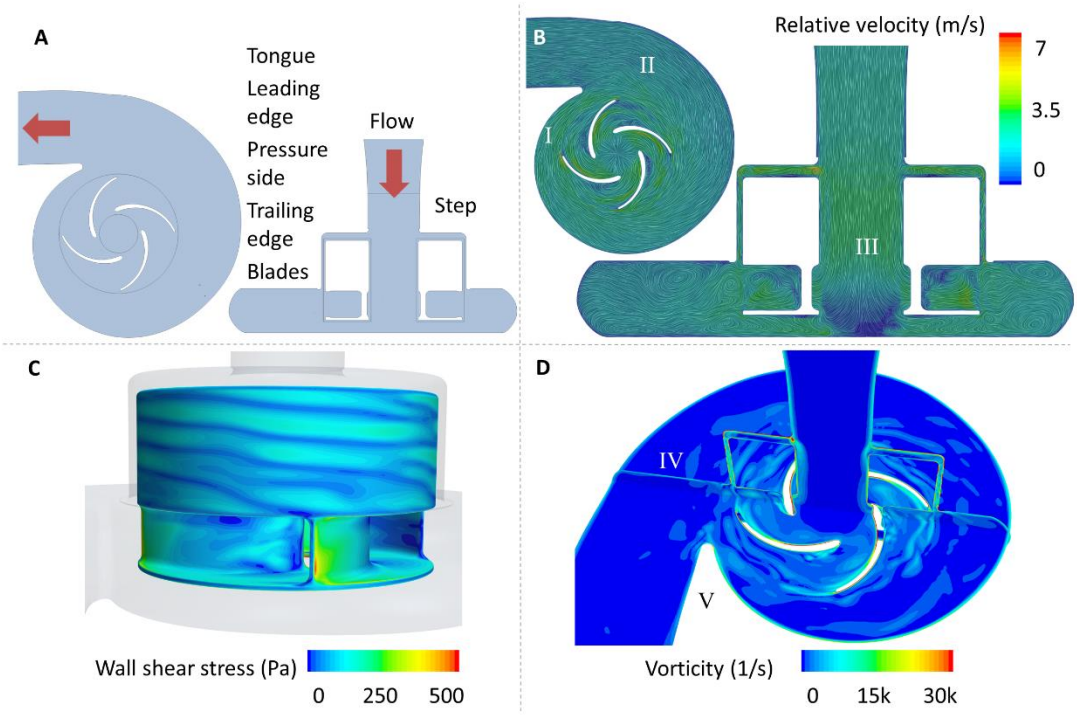

Figure 2: General characteristics of the HM3 hemodynamics in the 'baseline' scenario. A: Geometry features. B: Relative velocity. Here, 'relative' refers to the coordinate system: velocity with respect to the rotating coordinate system in the rotating part and relative to the laboratory system in the stationary part. Areas of flow detachment are observed at the pressure sides (I) and the trailing edges (II) of the blades. An area of stagnation forms centrally under the rotor (III). C. Wall shear stress (WSS) on the rotor surface. Highest WSS occurs at the trailing edges. In the gap, a WSS pattern caused by wavy vortex-like flow is observed. D. Vorticity is increased in regions of recirculation or flow detachment at the pressure side and trailing edges of the blade, in the gap (IV), as well as at the tongue (V), depending on blade position.

Next, we explored the influence of unsteady pump operation. In the 'cardiac cycle' scenario, some destabilization occurs during systole (Figure 3A). The area of low flow under the rotor shifts towards the outlet during high flow.

The speed decrease of the artificial pulse severely destabilizes the flow, leading to multiple vortices (Figure 3B). Vortices form in the blade channels and centrally between their leading edges. Vortical structures are particularly present close to the rotating body and travel towards the inlet cannula during backflow. The subsequent speed increase leads to an overall stabilization of the flow. The final speed change from top speed back to nominal leads to the anticipated overall reduction of velocities, but not to the formation of major vortices.

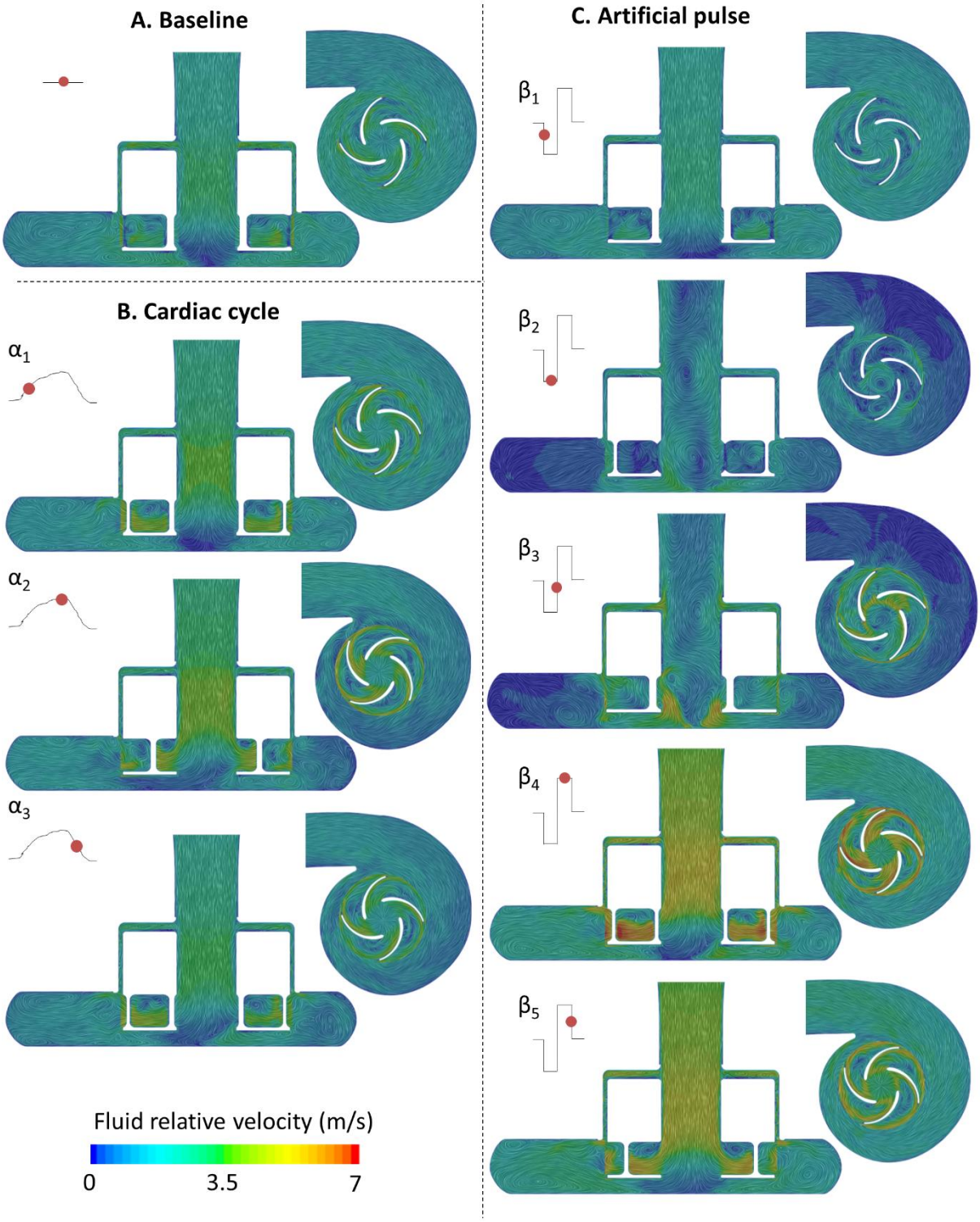

Figure 3: Relative velocities at selected time points α_1-α_4 (Panel A, 'cardiac cycle' scenario) and β_1-β_5 (Panel B, 'artificial pulse' scenario) as defined in Figure 1. Relative velocities are visualized in supplementary videos 1 to 6 for all scenarios.

Turbulence and vortical structures

Turbulence is suspected to influence blood damage [25]. Turbulence content is substantially higher in the 'artificial pulse' compared to the other two scenarios. Vortices build especially during deceleration of the rotor and low flow or backflow conditions, as highlighted in Figure 3.

Stresses

Since damage to blood components is caused, among other factors, by a combination of high stresses and exposure times [26], we assessed both Eulerian stress levels and computed heat maps visualizing time-dependent aspects.

In the 'baseline' scenario, highest viscous stresses are observed at the trailing edges, in the side gaps and at the transition from top gap to the main flow path (Figure 4A). Total stresses are highest in the blade channels and the narrowest part of the volute, while they are slightly elevated in the volute towards the outlet. In the 'cardiac cycle' scenario, overall viscous and total stress levels within the rotor increase. Peak total stresses are observed at the pressure side of the blades, the top part of the blade trailing edges and the tongue (Figure 4B). In the 'artificial pulse' scenario, viscous stress levels in the rotor decrease during the period of low flow and increase during high rotational speed (Figure 4C). Total stresses in the rotor and volute rise considerably during the period of low flow, and zones of elevated stresses are also located towards the inlet. At the time of the increase in rotor speed, large parts of the rotor experience total stresses > 100 Pa. Overall levels of total stress decrease only as the system returns to nominal conditions. The difference in total stress levels between the three investigated scenarios is also visualized in Figure 4D, where the fluid volume exposed to total stresses > 150 Pa is displayed.

A Lagrangian perspective allows the assessment of exposure times in addition to stress magnitudes, which is highlighted in Figure 5. Table 1 summarizes the fraction of particles exposed to stresses above thresholds of 9, 50 and 150 Pa, which have been suggested to be indicative of different types of blood damage [26] and are useful as comparative metrics between different operating conditions or pump designs [27].

In the 'cardiac cycle' scenario, the fraction of particles exposed to viscous and total stresses above 50 and 150 Pa (Table 1) as well as the corresponding exposure times (Figure 5, B2 and B3) are similar, highlighting the small contribution of Reynold stresses. For the artificial pulse case, total stresses are considerably higher than viscous ones, resulting in a shift to higher total stress values and longer exposure times (Figure 5, C3). This is also reflected in the increased number of particles exposed to total stresses above the selected threshold as compared to viscous stresses (Table 1).

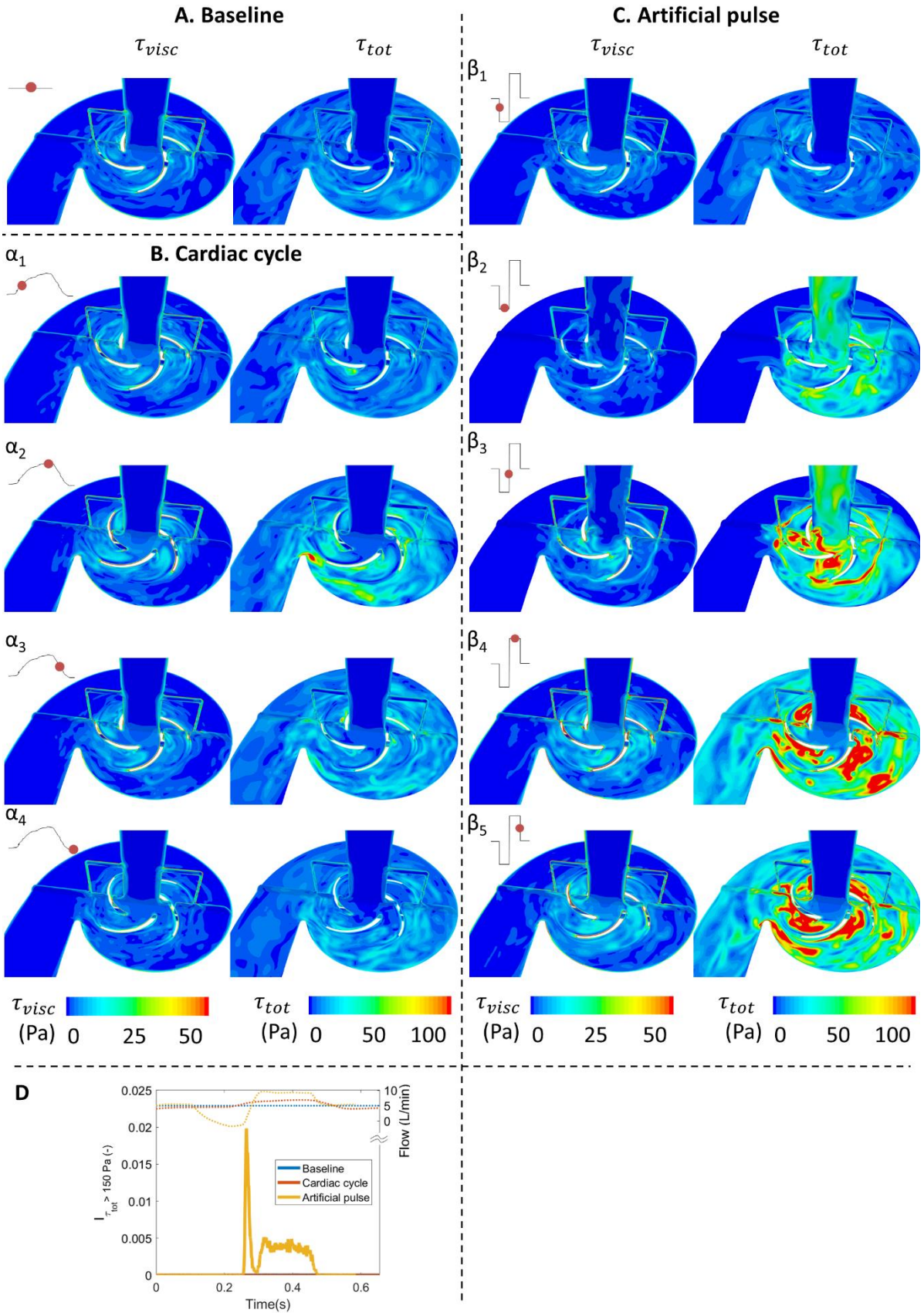

Figure 4: Viscous and total stresses in the 'baseline' (Panel A), 'cardiac cycle' (Panel B) and 'artificial pulse' scenarios (Panel C) at selected time points as defined in Figure 1. Note the different scales for viscous and total stresses. D: Fraction of fluid volume with τ_{tot} > 150 Pa. Values for the 'baseline' and 'cardiac cycle' scenarios are $1.9 \cdot 10^{-5}$ and $1.6 \cdot 10^{-5}$, respectively, thus too small to be visible here. The pump flow rates, plotted with dotted lines, are included to aid with interpretation (values on right vertical axis).

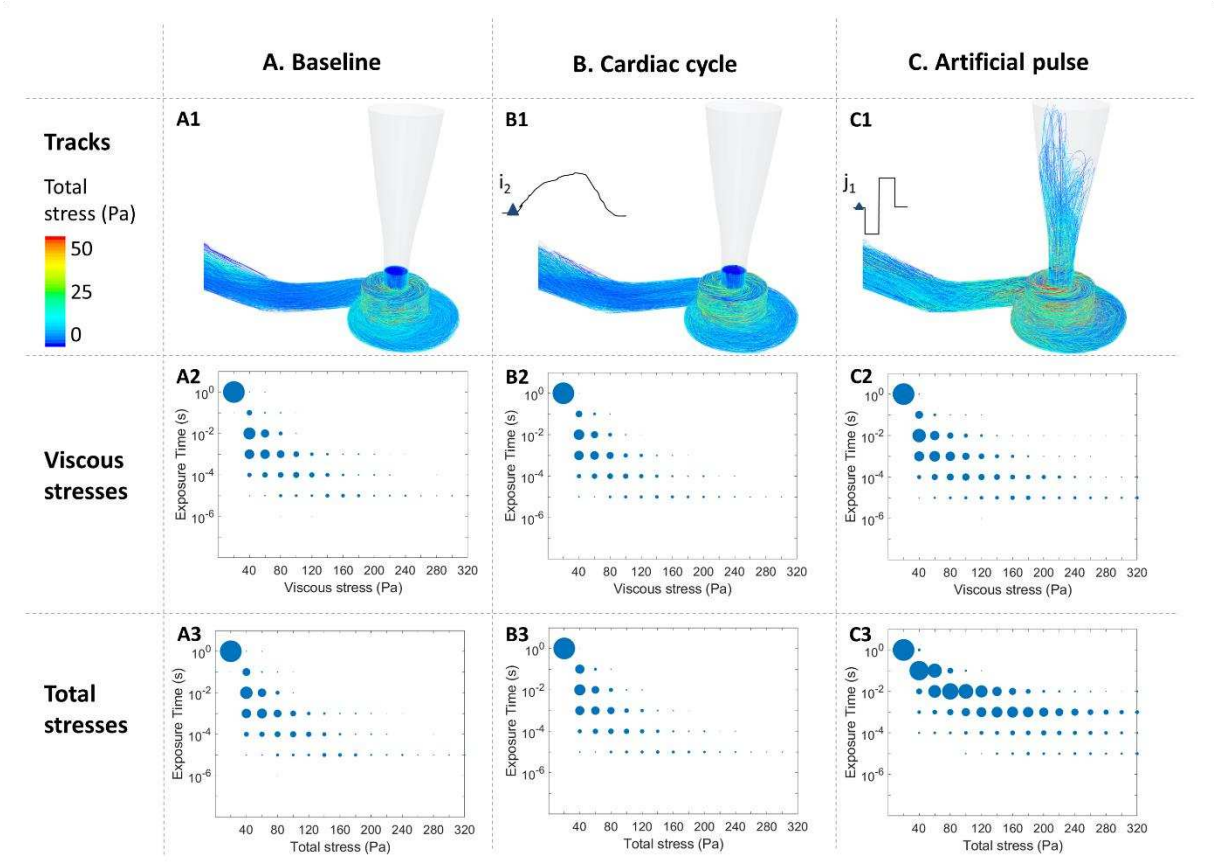

Figure 5: Lagrangian track data in the 'baseline' (Panels A), 'cardiac cycle' (Panels B) and 'artificial pulse' scenarios (Panels C). Panels 1: Particle tracks are colored according to the experienced total stress. In all cases, particles are injected on the same plane. I_2 and j_1 indicate the corresponding injection point for the Lagrangian particles. For the artificial pulse case, the effect of backflow is evident as the particles are advected back towards the inlet. Panels 2: Heat maps of exposure times and viscous stresses. The stresses are binned in intervals of 20 Pa (e.g. 100 Pa < τ < 120 Pa), and the exposure time of each track to levels of stress in each bin is calculated. The exposures times are then binned in a logarithmic manner (e.g. 10^{-3} < t < 10^{-2}). The sizes of the circles represent the number of entries per time and stress bin. Panels 3: Heat maps of exposure times and total stresses. In this figure, only the results of one set of tracks are displayed per simulation. The respective injection times are indicated in B1 and C1. Results for the other sets of tracks look qualitatively similar and are available in supplementary figures 9 and 10.

	Viscous stresses			Total stresses		
	Baseline (%)	Cardiac cycle (%)	Artificial pulse (%)	Baseline (%)	Cardiac cycle (%)	Artificial pulse (%)
$\tau_{thres} = 9\ Pa$	83	81	88	99	99	100
$\tau_{thres} = 50\ Pa$	34	30	40	36	37	90
$\tau_{thres} = 150\ Pa$	5	5	10	5	5	39

Table 1: Fraction of particles (%) exposed to $\tau > \tau_{thres}$ in the 'baseline', 'cardiac cycle' and 'artificial pulse' scenarios. For the 'cardiac cycle' and the 'artificial pulse' scenarios, the numbers represent the arithmetic mean of the fraction of exposed particles across all sets of tracks. 'Exposed particles' refers to particles that were exposed to stresses above the threshold at least once. Each set of particle tracks corresponds to one injection time (as highlighted in Figure 1), and the individual values per injection time are reported in the supporting information.

Washout

To test washout behavior, which is presumably relevant for thrombus formation, we analyzed the relative content of a passive scalar. We found that scalar washout of the HM3 is generally good (95% washout after 26 rotations in the cardiac cycle case, Figure 6A), including also the stagnation area below the rotor observed during constant pump operation (Figure 2A). However, there remains a detachment area with poor washout downstream of the kink in the outlet graft (Figure 6B). In the 'artificial pulse' scenario, backflow leads to particle movement in reverse direction towards the inlet, and increases the time until the passive scalar has left the domain. Washout is visualized in supplementary videos 7 to 9.

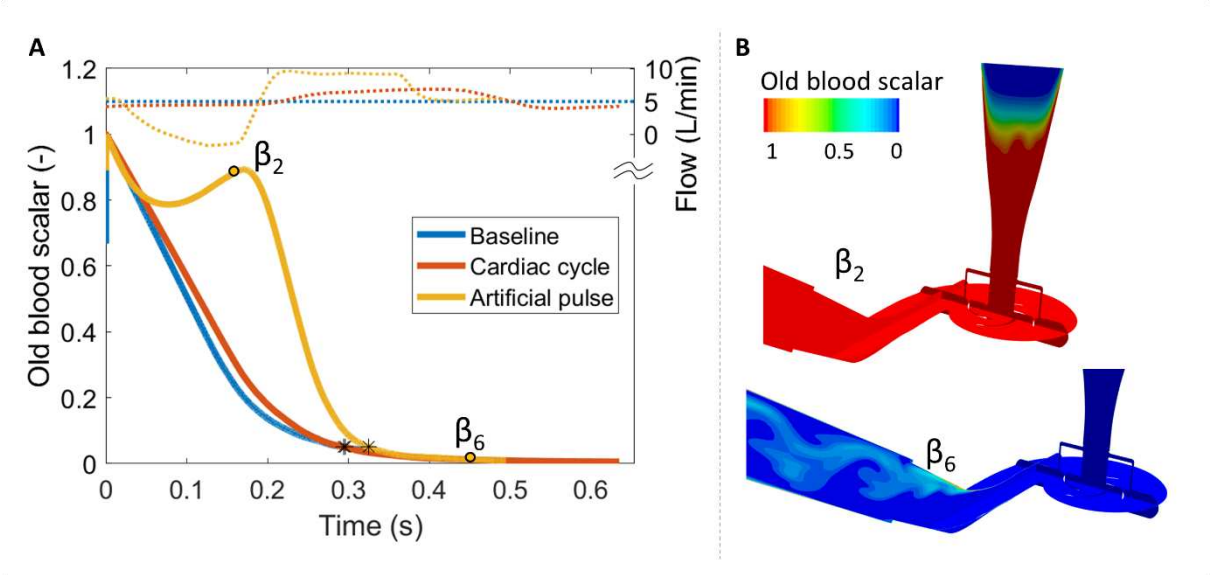

Figure 6: Passive scalar washout. A. Relative content of the passive scalar (labeled 'Old blood scalar') in the domain. The asterisks indicate the time point of 95% washout. The time scale is relative to the time point of initialization of the passive scalar. The pump flow rate is plotted with dotted lines to aid interpretation (values on right vertical axis). B. Visualizations of old blood scalar content at two selected time points (β_2, β_6) as defined in Figure 1.

Stagnation and recirculation

Since zones of stagnation and recirculation negatively affect hemocompatibility, we qualitatively and quantitatively assessed their extent. In the 'baseline' scenario, areas of stagnation are observed at the small step (labelled as "Step" in Figure 2A) at the transition site from inlet cannula to volute (Figure 7A, I), at the end of the secondary flow path (II), centrally under the rotor (III), at the bottom of the rotor close to the inner edge (IV) and at the volute wall (V). In the 'cardiac cycle' scenario, the extent of low velocity zones ($v < 0.2$ m/s) remains relatively constant (Figure 7B-C), whereas in the 'artificial pulse' scenario, the volumes of low velocity peak to 12 times the 'baseline' scenario value during backflow conditions and almost vanish at high rotor speed (Figure 7C-E).

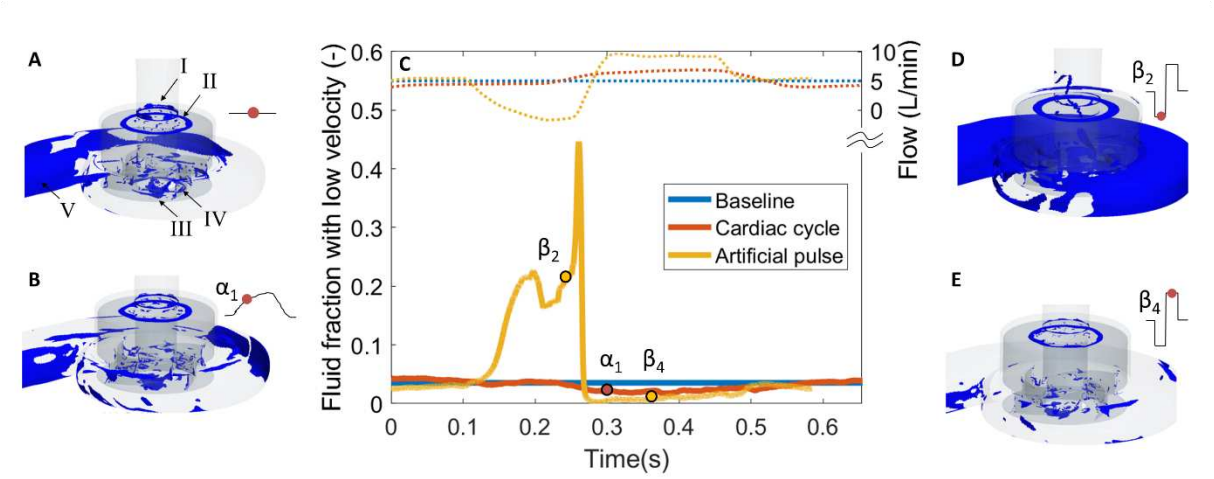

Figure 7: Regions of low velocity: volume with v_{rel} < 0.2 m/s and distance from walls > 40 µm. A. 'Baseline' scenario. Blue areas indicate volumes of low velocity. The black arrows indicate areas of stagnation: at the small geometry step at the transition from inlet cannula to volute (I), at the end of the secondary flow path (II), centrally under the rotor (III), at the bottom of the rotor close to the inner edge (IV) and at the volute wall (V). B. Situation during systole in the 'cardiac cycle' scenario. C. Fluid fraction with low velocity plotted over time for the three investigated scenarios. The pump flow rate is plotted with dotted lines to aid interpretation (values on right vertical axis). D. Situation during low speed in the 'artificial pulse' scenario. E. Situation during high speed in the 'artificial pulse' scenario. The selected time points (α_1, β_2 and β_4) refer to those defined in Figure 1. Videos of the regions of low velocity are available as supplementary videos 10 to 12.

Validation

To validate the CFD simulations, we compared the simulated hydraulic performance of the pump to values measured in vitro. We assessed the modelled pressure head for a specified flow for 7 operating conditions at 3 different speeds. Simulated pressures were in good agreement with experimental measurements with relative errors ranging between 0.7% and 13.6% (Figure 8).

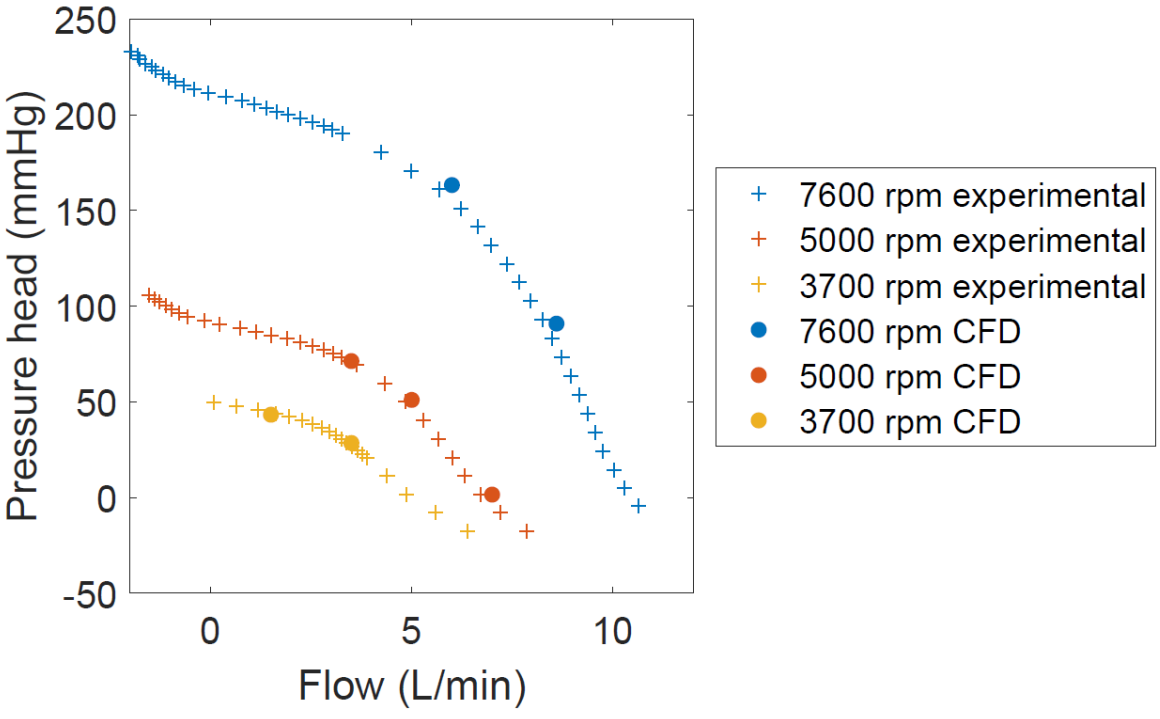

Figure 8: HQ plot displaying measured data and CFD simulation results. H: pressure head (mmHg), Q: flow rate (L/min)

Discussion

We carried out a high-resolution analysis of the flow inside the HM3 under dynamic conditions, and explored the fluid dynamic effects of its artificial pulse feature, a periodic modulation of the pump rotational speed intended to enhance pump washout as well as to partially restore arterial pulsatility [1]. We compared the effect of the HM3 artificial pulse on the flow field to that induced by the remaining cardiac function. Our high-resolution CFD simulations with dynamic boundary conditions allow for unprecedented insight into this VAD's transient flow structures, such as temporal evolution of low velocity and high shear regions. This is of relevance for assessing washout and thrombus formation potential, and determining effective stress and exposure time profiles during physiological off-design point operation. In contrast to the current calculations, previous numerical investigations of axial or centrifugal VADs have employed moving reference frame approaches or large time-steps [28,29], precluding the continuous analysis of flow structures, or have relied on small time steps but used static boundary conditions [30,31].

Clinical experience to date suggests that while the HM3 significantly outperforms previous devices in terms of the occurrence of pump thrombosis, patients still suffer from similar rates of gastrointestinal bleeding and detrimental stroke [2]. From a fluid dynamic perspective, this shifts two phenomena into the spotlight: supra-physiological stresses for their potential to damage blood cellular and non-cellular components, as well as stagnation and recirculation regions for their role in thrombus formation and growth.

Elevated stresses affect erythrocytes, platelets, leucocytes and blood proteins, thereby causing hemolysis, platelet activation and impairment of VWF function, respectively. Experimentally determined stress thresholds for hemolysis depend on exposure time, but are generally above 150 Pa [32]. However, recent evidence suggests that even subclinical hemolysis, which may occur below the above mentioned thresholds, might contribute to thrombotic adverse events [33]. Since viscous stresses in the HM3 are generally lower than 150 Pa throughout the investigated conditions, we expect negligible hemolysis, which fits clinical experience [2] and in-vitro experiments [1]. What could occur is subclinical hemolysis, possibly causing a procoagulant state. Shear-mediated platelet activation has been studied experimentally [34–36]. Applying the power-law model postulated in [34], our calculations indicate a platelet activation state below 1% in the HM3 for the observed viscous stresses and exposure times. However, platelet activation is also sensitive to stress gradients, and high-frequency components (here: 82-94 Hz) have been shown to be major triggers for activation [36]. Analysis of our particle tracks revealed that they often contain frequencies in or above the high-frequency range investigated in [36], suggesting that we may expect higher damage than predicted by the simple power-law model. Shear-mediated damage has further been shown to be a main driver of acquired von Willebrand syndrome (avWs), which is associated with the bleeding problems in VAD patients [37]. The exact relationship between shear exposure and bleeding has not yet been found, but experimental studies suggest that stress of the levels seen in the HM3 would, indeed, damage the VWF [7,38]. Aspects not included in experimental studies so far are damage accumulation and relaxation: Since blood components pass through the high shear environment inside the implanted device thousands of times, damage accumulation and relaxation between exposures could take place. It is known that the stress history should be taken into account to accurately predict potential damage [39]. Consequently, experimental results obtained for long, but single exposures (minutes in [36], hours in [7,38]) might still be translatable to the clinical setting, but it is not clear how such translation should be done. An additional challenge in the translation of in-silico or in-vitro data to the clinical situation is the hematologic state of the patients before VAD implantation. It has been shown that acute heart failure patients show increased levels of interleukin-6, which might contribute to the

prothrombotic state of these patients [40]. At the same time, some patients suffer from avWs already before VAD implantation, which might predispose them to bleeding events [41].

There is evidence that turbulent flow situations lead to higher blood trauma than laminar flows with comparable levels of viscous stresses [25]. We accommodated that fact by considering both viscous and total stress levels. Overall, viscous stresses in the HM3 are lower than in the HM2 and the HVAD [42] (see supporting information). Viscous stress levels are also generally lower in the investigated 'cardiac cycle' scenario than in the 'artificial pulse' one. For example, approximately 30% of all particles are exposed to viscous stresses > 50 Pa in the former scenario, and approximately 40% in the latter. Due to the transient flow reversal, exposure times to given viscous shear stress levels are also slightly longer in the 'artificial pulse' scenario (Figure 5, B2 and C2). Yet, the most notable differences are observed in the total stress levels. Total stresses within the cardiac cycle remain similar to viscous stresses, highlighting limited turbulence levels and a small contribution of Reynold stresses. In contrast, in the 'artificial pulse' scenario, total stress levels and the respective exposure times are substantially higher than the viscous ones (Figure 5, C2 and C3). Approximately 37% of the seeded particles are exposed to total stresses > 50 Pa in the 'cardiac cycle' scenario, while in the 'artificial pulse' one 90% of the particles seeded during or shortly before the pulse are affected. Since the artificial pulse covers only 17.5% of the HM3's runtime [1], this translates to approximately 44% of the particles being exposed to total stresses > 50 Pa assuming baseline conditions outside the pulse sequence. The biological effect of Reynold stresses on cells is still a matter of debate. While initially it was believed that Reynold stresses damage blood directly [43,44], it was later argued that Reynold stresses are inappropriate for direct assessment of mechanical load on cells and that, instead, the resulting viscous stresses should be estimated [32,45]. In conclusion, the strong increase in total stresses during the artificial pulse should certainly be kept in mind, but further research is needed to understand its potential implications for hemocompatibility and clinical outcome.

Independent of the possible consequences, the artificial pulse significantly increased the modelled turbulence in the system. Flow reversal, which may not happen in all patients, reinforces the destabilization observed after initial deceleration of the flow. However, the strongest turbulent onset is clearly associated with the rapid speed increase by 4000 rpm following the period of very low flow. This is highlighted by the increased total stress levels (Figure 4), and might be important to consider during the design of artificial pulse features in general. Investigations of the impact of artificial pulses with different characteristics on clinical outcome would be of great value to that end.

Beyond stresses, detrimental flow features include zones of flow detachment, which were observed at the pressure sides and trailing edges of the blades independent of blade position during all (quasi-) static situations assessed in this study. In the 'cardiac cycle' scenario, the detached zones close to the blades remained stable, while the zone under the rotor shifted and resolved during peak flow (supplementary videos 3, 4 and 11). The extent of these changes will depend on individual remaining cardiac function. In the 'artificial pulse' scenario, the low speed caused overall low velocities, but resolved all stagnation and recirculation zones. These zones of stagnation and recirculation are prone for thrombus growth and generally decrease the hydraulic efficiency of the pump, thus a design minimizing their extent is favorable.

Good passive scalar washout performance was observed for all investigated scenarios. It therefore appears that washout is governed largely by the device geometry and pump flow rate. The time required for 95% washout was comparable to that found in the HVAD, which features a secondary flow path similar to the HM3 [46]. Notably, the implemented scalar only characterizes washout of a fully soluble quantity, neglecting effects like mechanical interaction with the wall or biological interaction between blood components. It is thus conceivable that although the artificial pulse does not increase

scalar washout, it may, in reality, help remove blood components from pump surfaces by inducing the observed drastic changes in the flow field and wall shear stress (WSS). When interpreted in this way, our results align well with clinical observations of very small numbers of pump thrombi in the HM3 [2].

An important aspect in VADs is pulsation or the lack thereof in rotary blood pumps [47]. Speed modulations as in the HM3 or in the HVAD [9] are a way to induce pulsatility. The speed modulation studied herein resulted in a larger pressure pulse than the corresponding contribution of the residual cardiac function (11 vs 5 mmHg). However, it has to be kept in mind that the artificial pulse is not synchronized with the patient's cardiac cycle. While we have shown here clearly that the artificial pulse has a substantial effect on the flow field, its biological and clinical implications remain to be resolved.

The computational approach employed in this study comes with limitations. Since the geometry is reverse-engineered, small differences to the actual geometry cannot be excluded. Specifically, even small differences in the gap between rotor and housing can influence the obtained stress fields [27]. Here, the rotor position is assumed to be fixed at all operating points. Due to the passive magnetic bearing in the axial direction, the gap might change with changing operating conditions. Furthermore, we assumed rotor actuation to be perfect, implying that the rotor speed always equals its set speed. In our simulations, walls were assumed to be smooth in contrast to the partly sintered actual device. Sintered surfaces may lead to higher stresses than predicted here and could slightly reduce efficiency. Also, even though the turbulence modelling employed in this study follows best practices, it still remains an approximation. Detailed measurements of the turbulent structures in VADs have not been obtained to date. Since the artificial pulse feature is not synchronized with the heartbeat, the flow and pressure dynamics vary considerably depending on the relative temporal position of native and artificial pulse (periodicity > 66s for 91.2 bpm), which makes CFD simulations of scenarios including both the native heart function and the artificial pulse feature too costly. However, we have investigated such a combination using our LP model. We found that we can capture the characteristics of the pressure and flow curves of a combined case using our 'cardiac cycle' and 'artificial pulse' scenarios. In our CFD model, pressure curves are prescribed as BCs, and govern the occurring flow structures. Thus, while it is not feasible to run the full CFD of the combined native cardiac cycle and the artificial pulse, we expect that the flow patterns therein will not be fundamentally different to what we observed in the two isolated cases. Consequently, we believe that the here presented results will aid in understanding clinically relevant flow patterns in the HM3 (see supporting information). It must also be noted that the flow fields formed during the artificial pulse feature, and especially possible flow reversals, depend on pump speed, pressure head and likely on individual patient physiology.

Conclusion

Our analysis of the fluid dynamics in the HM3 under dynamic physiologic conditions indicates good washout, which is in line with the clinical observation of very low pump thrombus occurrence rates. Viscous stress levels are slightly higher during the device's artificial pulse, but overall lower than in other clinically used VADs. However, these stress levels are still above what is currently considered benign, which may be reflected in the clinically observed rates of stroke and bleeding, presumably caused, among other factors, by damage to platelets. In our simulations, the artificial pulse did not substantially affect washout, but sudden changes in WSS may aid removal of potential deposits in the pump. At the same time, the artificial pulse increased turbulence substantially. While the biologic effects of turbulence are not known in detail, the resulting elevated total stresses might contribute to hemocompatibility-related problems observed in the clinics.

Acknowledgements

The authors gratefully acknowledge the financial support provided by the Swiss National Science Foundation through grant 200021_147193 CINDY and NCCR Kidney.CH, the University of Zurich through Forschungskredit grant FK-17-040, and the Stavros Niarchos Foundation. This work is part of the Zurich Heart project under the umbrella of University Medicine Zurich.

Author contributions

L.W., D.D.Z, B.T. and V.K. designed the study. B.T. reconstructed the device geometry. L.W. carried out the CFD calculations. L.W., B.T and D.D.Z analyzed the CFD data. M.G. established the lumped parameter model. S.B. performed the in vitro measurements. L.W., D.D.Z., B.T and M.G. interpreted the results. L.W., D.D.Z and V.K. wrote the manuscript. M.S.D., M.M. and V.K. secured funding and directed the research. All authors critically reviewed and approved the manuscript.

References

1. Bourque K, Cotter C, Dague C, Harjes D, Dur O, Duhamel J, et al. Design Rationale and Pre-Clinical Evaluation of the HeartMate 3 Left Ventricular Assist System for Hemocompatibility. ASAIO J. 2016;62:375–83.

2. Mehra MR, Goldstein DJ, Uriel N, Cleveland JC, Yuzefpolskaya M, Salerno C, et al. Two-Year Outcomes with a Magnetically Levitated Cardiac Pump in Heart Failure. N. Engl. J. Med. 2018;378:1386–95.

3. Rogers JG, Pagani FD, Tatooles AJ, Bhat G, Slaughter MS, Birks EJ, et al. Intrapericardial Left Ventricular Assist Device for Advanced Heart Failure. N. Engl. J. Med. 2017;376:451–60.

4. Netuka I, Kvasnička T, Kvasnička J, Hrachovinová I, Ivák P, Mareček F, et al. Evaluation of von Willebrand factor with a fully magnetically levitated centrifugal continuous-flow left ventricular assist device in advanced heart failure. J. Hear. Lung Transplant. 2016;35:860–7.

5. Hochareon P, Manning KB, Fontaine A a, Tarbell JM, Deutsch S. Correlation of in vivo clot deposition with the flow characteristics in the 50 cc penn state artificial heart: a preliminary study. ASAIO J. 2004;50:537–42.

6. Hellums JD. 1993 Whitaker lecture: Biorheology in thrombosis research. Ann. Biomed. Eng. 1994;22:445–55.

7. Bartoli CR, Restle DJ, Zhang DM, Acker MA, Atluri P. Pathologic von Willebrand factor degradation with a left ventricular assist device occurs via two distinct mechanisms: Mechanical demolition and enzymatic cleavage. J. Thorac. Cardiovasc. Surg. Elsevier Inc.; 2015;149:281–9.

8. Moazami N, Dembitsky WP, Adamson R, Steffen RJ, Soltesz EG, Starling RC, et al. Does pulsatility matter in the era of continuous-flow blood pumps? J. Hear. Lung Transplant. Elsevier; 2015;34:999–1004.

9. Zimpfer D, Strueber M, Aigner P, Schmitto JD, Fiane AE, Larbalestier R, et al. Evaluation of the HeartWare ventricular assist device Lavare cycle in a particle image velocimetry model and in clinical practice. Eur. J. Cardio-thoracic Surg. 2016;50:839–48.

10. Gupta S, Woldendorp K, Muthiah K, Robson D, Prichard R, Macdonald PS, et al. Normalisation of haemodynamics in patients with end-stage heart failure with continuous-flow left ventricular assist

device therapy. Hear. Lung Circ. Australian and New Zealand Society of Cardiac and Thoracic Surgeons (ANZSCTS) and the Cardiac Society of Australia and New Zealand (CSANZ); 2014;23:963–9.

11. Thamsen B, Plamondon M, Granegger M, Schmid Daners M, Kaufmann R, Neels A, et al. Investigation of the Axial Gap Clearance in a Hydrodynamic-Passive Magnetically Levitated Rotary Blood Pump Using X-Ray Radiography. Artif. Organs. 2018;00:0–5.

12. Merrill EW. Rheology of blood. Physiol. Rev. 1969;49:836–86.

13. Colacino FM, Moscato F, Piedimonte F, Arabia M, Danieli GA. Left ventricle load impedance control by apical VAD can help heart recovery and patient perfusion; a numerical study. ASAIO J. 2007;53:263–77.

14. Burkhoff D, Maurer MS, Joseph SM, Rogers JG, Birati EY, Rame JE, et al. Left Atrial Decompression Pump for Severe Heart Failure With Preserved Ejection Fraction: Theoretical and Clinical Considerations. JACC Hear. Fail. 2015;3:275–82.

15. Fresiello L, Meyns B, Di Molfetta A, Ferrari G. A model of the cardiorespiratory response to aerobic exercise in healthy and heart failure conditions. Front. Physiol. 2016;7:1–17.

16. Moscato F, Wirrmann C, Granegger M, Eskandary F, Zimpfer D, Schima H. Use of continuous flow ventricular assist devices in patients with heart failure and a normal ejection fraction: a computer-simulation study. J. Thorac. Cardiovasc. Surg. 2013;145:1352–8.

17. Westerhof N, Lankhaar J-W, Westerhof BE. The arterial Windkessel. Med. Biol. Eng. Comput. 2009;47:131–41.

18. Hayward CS, Kalnins W V, Rogers P, Feneley MP, Macdonald PS, Kelly RP. Left Ventricular Chamber Function During Inhaled Nitric Oxide in Patients with Dilated Cardiomyopathy. J. Cardiovasc. Pharmacol. 1999;34.

19. Granegger M, Moscato F, Casas F, Wieselthaler G, Schima H. Development of a pump flow estimator for rotary blood pumps to enhance monitoring of ventricular function. Artif. Organs. 2012;36:691–9.

20. Moscato F, Danieli GA, Schima H. Dynamic modeling and identification of an axial flow ventricular assist device. Int. J. Artif. Organs. 2009;32:336–43.

21. Ochsner G, Amacher R, Amstutz A, Plass A, Schmid Daners M, Tevaearai H, et al. A novel interface for hybrid mock circulations to evaluate ventricular assist devices. IEEE Trans. Biomed. Eng. 2013;60:507–16.

22. Cohn WE, Gregoric ID, Frazier OH. Reinforcement of Left Ventricular Assist Device Outflow Grafts to Prevent Kinking. Ann. Thorac. Surg. 2007;84:301–2.

23. Bludszuweit C. Three Dimensional Numerical Prediction of Stress Loading of Blood Particles in a Centrifugal Pump. Artif. Organs. 1995;19:590–6.

24. Faghih MM, Sharp MK. Extending the Power-Law Hemolysis Model to Complex Flows. J. Biomech. Eng. 2016;138:124504.

25. Kameneva M V, Burgreen GW, Kono K, Repko B, Antaki JF, Umezu M. Effects of turbulent stresses upon mechanical hemolysis: experimental and computational analysis. ASAIO J. 2004;50:418–23.

26. Fraser KH, Zhang T, Taskin ME, Griffith BP, Wu ZJ. A Quantitative Comparison of Mechanical Blood Damage Parameters in Rotary Ventricular Assist Devices: Shear Stress, Exposure Time and Hemolysis Index. J. Biomech. Eng. 2012;134:081002.

27. Wiegmann L, Boës S, de Zélicourt D, Thamsen B, Schmid Daners M, Meboldt M, et al. Blood Pump

Design Variations and Their Influence on Hydraulic Performance and Indicators of Hemocompatibility. Ann. Biomed. Eng. 2018;46:417.

28. Song X, Wood HG, Olsen D. Computational Fluid Dynamics (CFD) study of the 4th generation prototype of a continuous flow Ventricular Assist Device (VAD). J. Biomech. Eng. 2004;126:180–7.

29. Chen Z, Jena SK, Giridharan GA, Koenig SC, Slaughter MS, Griffith BP, et al. Flow features and device-induced blood trauma in CF-VADs under a pulsatile blood flow condition: A CFD comparative study. Int. j. numer. method. biomed. eng. 2018;34:e2924.

30. Song X, Throckmorton AL, Wood HG, Allaire PE, Olsen DB. Transient and quasi-steady computational fluid dynamics study of a left ventricular assist device. ASAIO J. 2004;50:410–7.

31. Masuzawa T, Ohta A, Tanaka N, Qian Y, Tsukiya T. Estimation of changes in dynamic hydraulic force in a magnetically suspended centrifugal blood pump with transient computational fluid dynamics analysis. J. Artif. Organs. 2009;12:150–9.

32. Quinlan NJ, Dooley PN. Models of flow-induced loading on blood cells in laminar and turbulent flow, with application to cardiovascular device flow. Ann. Biomed. Eng. 2007;35:1347–56.

33. Bartoli CR, Zhang D, Kang J, Hennessy-Strahs S, Restle D, Howard J, et al. Clinical and In Vitro Evidence That Subclinical Hemolysis Contributes to LVAD Thrombosis. Ann. Thorac. Surg. The Society of Thoracic Surgeons; 2017;

34. Ding J, Chen Z, Niu S, Zhang J, Mondal NK, Griffith BP, et al. Quantification of Shear-Induced Platelet Activation: High Shear Stresses for Short Exposure Time. Artif. Organs. 2015;39:576–83.

35. Sheriff J, Soares JS, Xenos M, Jesty J, Bluestein D. Evaluation of shear-induced platelet activation models under constant and dynamic shear stress loading conditions relevant to devices. Ann. Biomed. Eng. 2013;41:1279–96.

36. Consolo F, Sheriff J, Gorla S, Magri N, Bluestein D, Pappalardo F, et al. High Frequency Components of Hemodynamic Shear Stress Profiles are a Major Determinant of Shear-Mediated Platelet Activation in Therapeutic Blood Recirculating Devices. Sci. Rep. 2017;7.

37. Nascimbene A, Neelamegham S, Frazier OH, Moake JL, Dong J. Acquired von Willebrand syndrome associated with left ventricular assist device. 2016;127:3133–42.

38. Houng H, Chan C, Pieper IL, Hoi C, Chan H, Pieper IL, et al. The Effect of Shear Stress on the Size , Structure , and Function of Human von Willebrand Factor. Artif. Organs. 2014;38:741–50.

39. Bluestein D. Towards optimization of the thrombogenic potential of blood recirculating cardiovascular devices using modeling approaches. Expert Rev. Med. Devices. 2006;3:267–70.

40. Chin BSP, Conway DSG, Chung NAY, Blann AD, Gibbs CR, Lip GYH. Interleukin-6, tissue factor and von Willebrand factor in acute decompensated heart failure: relationship to treatment and prognosis. Blood Coagul. Fibrinolysis. 2003;14.

41. Feldmann C, Zayat R, Goetzenich A, Aljalloud A, Woelke E, Maas J, et al. Perioperative onset of acquired von Willebrand syndrome: Comparison between HVAD, HeartMate II and on-pump coronary bypass surgery. PLoS One. 2017;12:1–17.

42. Thamsen B, Blümel B, Schaller J, Paschereit CO, Affeld K, Goubergrits L, et al. Numerical Analysis of Blood Damage Potential of the HeartMate II and HeartWare HVAD Rotary Blood Pumps. Artif. Organs. 2015;39:651–9.

43. Lu PC, Lai HC, Liu JS. A reevaluation and discussion on the threshold limit for hemolysis in a turbulent shear flow. J. Biomech. 2001;34:1361–4.

44. Sallam AM, Hwang NH. Human red blood cell hemolysis in a turbulent shear flow: contribution of Reynolds shear stresses. Biorheology. Netherlands; 1984;21:783–97.

45. Ge L, Dasi LP, Sotiropoulos F, Yoganathan AP. Characterization of hemodynamic forces induced by mechanical heart valves: Reynolds vs. viscous stresses. Ann. Biomed. Eng. 2008;36:276–97.

46. Molteni A, Masri ZPH, Low KWQ, Yousef HN, Sienz J, Fraser KH. Experimental measurement and numerical modelling of dye washout for investigation of blood residence time in ventricular assist devices. Int. J. Artif. Organs. 2018;

47. Mehra MR. The burden of haemocompatibility with left ventricular assist systems: a complex weave. Eur. Heart J. 2017;1–5.

Supplementary Information

Supplementary Information, pdf document.

Figure S1. Section-planes and line-probes used for the time and grid independence studies.

Figure S2. Pressure, velocity and vorticity fields for the tested grid sizes.

Figure S3. Pressure, velocity and vorticity fields for the tested time steps.

Figure S4. Dependence of velocity magnitude on grid size along the line probes.

Figure S5. Dependence of velocity magnitude on time step along the line probes.

Figure S6. Dependence of pressure on grid size along the line probes.

Figure S7. Dependence of pressure on time step along the line probes.

Figure S8. Dependence of shear stress on grid size along the line probes.

Figure S9. Dependence of shear stress on time step along the line probes.

Figure S10. Dependence of bulk indices on grid size.

Figure S11. Dependence of bulk indices on time step.

Figure S12. Lagrangian tracks independence study.

Figure S13. Viscous stress heat maps for all tested injection times.

Figure S14. Total stress heat maps for all tested injection times.

Figure S15. Comparison of fluid volumes exposed to viscous stresses over 9, 50 and 150 Pa in the HM3, HMII and HVAD.

Figure S16. Comparison of the distributions of viscous stress exposure in the HM3, HMII and HVAD.

Figure S17. Assessment of native cardiac cycle and artificial pulse combined.

Table S1. Fraction of particles exposed to viscous or total scalar stresses over 9, 50 and 150 Pa.

Supplementary Videos

Video S1: Relative velocities in the “baseline” scenario (radial plane).

Video S2: Relative velocities in the “baseline” scenario (axial plane).

Video S3: Relative velocities in the “cardiac cycle” scenario (radial plane).

Video S4: Relative velocities in the “cardiac cycle” scenario (axial plane).

Video S5: Relative velocities in the “artificial pulse” scenario (radial plane).

Video S6: Relative velocities in the “artificial pulse” scenario (axial plane).

Video S7: Passive scalar washout in the “baseline” scenario.

Video S8: Passive scalar washout in the “cardiac cycle” scenario.

Video S9: Passive scalar washout in the “artificial pulse” scenario.

Video S10: Regions of low velocities in the “baseline” scenario. Blue iso-surfaces enclose volumes with a relative velocity < 0.2 m/s and distance from walls >40 μm.

Video S11: Regions of low velocities in the “cardiac cycle” scenario. Blue iso-surfaces enclose volumes with a relative velocity < 0.2 m/s and distance from walls >40 μm.

Video S12: Regions of low velocities in the “artificial pulse” scenario. Blue iso-surfaces enclose volumes with a relative velocity < 0.2 m/s and distance from walls >40 μm.